AEROTHERMODYNAMIC ANALYSIS OF A SPACE VEHICLE FOR MANNED EXPLORATION MISSIONS TO MARS

A. Viviani*, G. Pezzella, C. Golia***
***Seconda Università di Napoli (SUN), via Roma 29, 81031 Aversa, Italy**
****Centro Italiano Ricerche Aerospaziali (CIRA), via Maiorise, 81043 Capua, Italy**

Keywords: *Planetary atmospheric reentry, Nonequilibrium flow, Aerothermochemistry, Aerodynamics.*

Abstract

This paper deals with the aerodynamic and aerothermodynamic analysis of a manned braking system entering the Mars atmosphere, with the aim of supporting planetary entry system design studies.
The effects of finite-rate chemistry and wall heterogeneous reactions on vehicle aerothermodynamics and aerodynamics are highlighted. Two vehicle configurations have been analyzed. A capsule configuration close to the Apollo one and a lifting body with a rounded edge delta-like cross section.
Several fully three-dimensional Computational Fluid Dynamics analyses, for perfect and non-equilibrium reacting gas approximations, have been performed to assess the flowfield environment around the vehicle. Hence, the aerodynamic and aerothermodynamic performance of the entry vehicle in the framework of a proposed Mars entry scenario is addressed. To this end, a wide range of flow conditions including different angles of attack, Mach and Reynolds numbers have been investigated and compared. Results show that real-gas effects influence both the aerodynamic drag and pitching moment, whereas the lift is only slightly affected.
Finally, comparison of results between non-catalytic and fully catalytic wall computations highlights that chemical reactions at vehicle surface play a significant role on the vehicle thermal load assessment.

1 Introduction

In this paper we report and discuss the results of design analyses of a Manned Braking System (MBS) entering the Mars atmosphere, with the aim of supporting design studies of a planetary entry system.

The human exploration of Mars will be a complex undertaking. It is an enterprise that will confirm the potential for humans to leave our home planet and make our way outward into the cosmos. Even if just a small step on a cosmic scale, it will be a significant one for humans, because it will require leaving Earth with very limited return capability [1], [2].

With this in mind, preliminary aerodynamic and aerothermodynamic analyses, performed for both an Apollo shaped and a lifting body vehicle, have been focused on in the paper for flight conditions compatible with a manned mission entering the Mars atmosphere. However, neither the mission architecture needed to reach Mars from Earth or neighbour Earth space, nor surface exploration have been addressed.

All the design analyses have been performed at several levels. Indeed, vehicle aerodynamic assessment has been extensively addressed through engineering-based design approach as, e.g., hypersonic panel methods (HPM); then, a number of fully three-dimensional Computational Fluid Dynamics (CFD) simulations, both with Euler and Navier-Stokes models, of the hypersonic flowfield past the entry vehicle have been performed.

The results, provided in this paper, consider a Mars entry scenario compliant with an approach to the red planet both by elliptic and hyperbolic orbit [1], [2]. These results may be used to provide numerical data for understanding requirements for the human exploration of Mars.

2 Mars Manned Entry Vehicle Layout

MBS configurations, under investigation in this work, are shown in Figure 1. The capsule configuration, named VP ARES C, is an axisymmetric blunt body, close to an Apollo shaped capsule, measuring about 5 m in diameter, with a nose radius of 6.05 m, a sidewall angle of 33 deg, and an overall height of 3.8 m. The lifting body, named VP ARES LB, features an aerodynamic configuration with a compact body about 8 metres long with a rounded edge delta-like cross section [3]. A very preliminary internal layout for a crew of four astronauts is also reported in Figure 1.

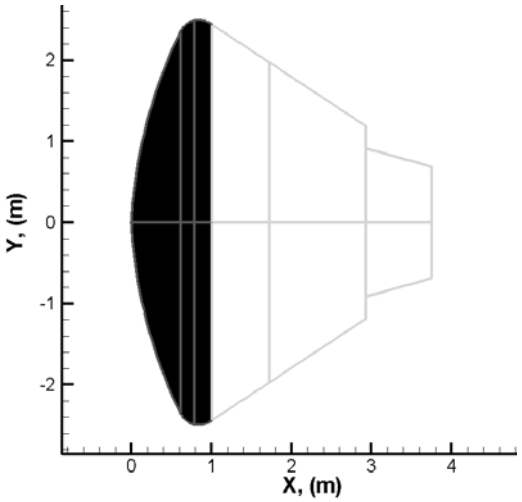

(a) Capsule - C

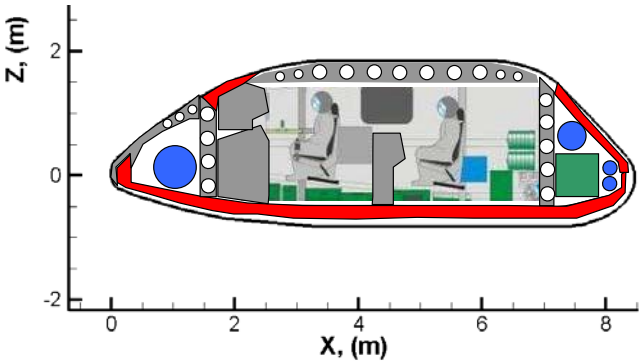

(b) Lifting Body - LB

Figure 1. *VP ARES configurations with quotes.*

3 Mars Entry Scenario

Generally speaking the MBS design depends on mission flight scenario requirements, which define vehicle entry corridor. Indeed, the entry corridor envelopes all the flyable/admissible entry trajectories whose loading environment is tolerable by the vehicle. It is bounded from one side by the heat flux peak and the maximum deceleration, from the other by the ablator thermal limitations (total heat load), if present, and the skip angle. The dispersion of the trajectory within the entry corridor depends on two main design parameters that are the entry flight path angle and velocity, which are characterized by the selected planetary approach trajectory. The angle and the velocity at entry interface determine the time of permanence in the Martian atmosphere. The shallower the entry angle, the longer the flight time and the dispersion due to the atmospheric model error, and, hence, the worse the landing accuracy. From the point of view of approach strategies, the different values of velocity at entry interface (given the entry angle) will characterize the MBS design by means of mechanical loads (i.e. pressure and acceleration), thermal loads (i.e. heat flux peak and integrated heat load), and landing dispersion [3], [4].

These parameters counterbalance with each other, in the sense that the higher the entry velocity (or the steeper the entry angle), the larger the deceleration during the descent path (higher structure solicitations) and, the higher the heat flux peak (higher thermal protection system –TPS– solicitations). Moreover, the lower the entry velocity (or the shallower the entry angle), the bigger the total heat flux (thicker ablative materials layer), the longer the atmospheric flight time, hence the higher the landing dispersion [5], [6].

The flight scenario considered so far is summarized in the altitude-velocity map in Figure 2. It refers to entry conditions compatible with a vehicle entering the Mars atmosphere both from a hyperbolic orbit (HO), e.g., direct planetary entry, and an elliptic orbit (EO).

As shown, both dynamic pressure peak (DPP) –filled triangle points– and peak heating (PH) –filled square points– on each entry trajectory are reported. VP ARES, flying along the descent trajectory by HO, reaches PH conditions at 52.06 Km altitude when the vehicle is travelling at about 4943 m/s (e.g., M_∞=26). On the contrary, PH conditions of

entry by EO are experimented when VP ARES is flying at M_∞=26 at 44.20 Km altitude.

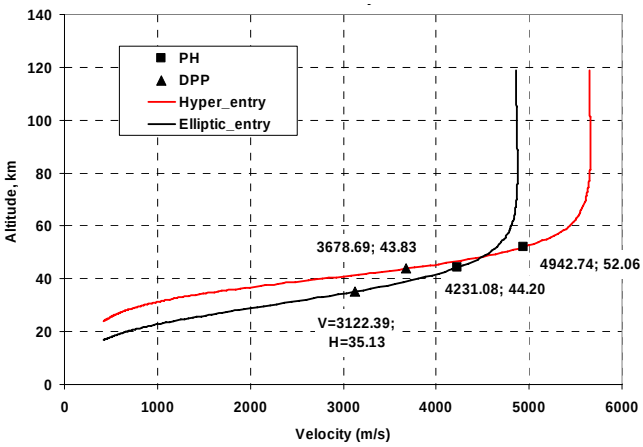

Figure 2. *MBS entry scenario for elliptic and hyperbolic entries.*

4 Design Analysis

CFD analyses have been performed to assess the aerothermal environment around the vehicle in order to evaluate several surface loading distributions (e.g. pressure and heat flux).

To this aim, several fully three-dimensional numerical computations, both for perfect and chemically reacting gas approximation, have been performed considering the entry scenario of Figure 2. Thirteen CFD numerical simulations have been performed at the freestream conditions and are listed in Table 1.

Table 1. *CFD freestream conditions*

		Mach [-]	AoA [deg]	Altitude [km]	CL [-]	CD [-]	CM* [-]
Perfect Gas		10	10	10.0	0.06150	0.13060	-0.03170
		15	40	60.0	0.47830	0.55360	-0.32940
		22	40	60.0	0.47930	0.55540	-0.33010
	EO PH	22	40	44.2	0.48300	0.55500	-0.33200
	HO PH	26	40	52.1	0.49920	0.55930	-0.34330
Reacting Gas		10	10	10.0	0.05710	0.12450	-0.02950
		10	20	10.0	0.19940	0.18730	-0.09930
		10	30	10.0	0.35970	0.33420	-0.20650
		10	40	10.0	0.49340	0.56100	-0.33770
EO PH	NCW	22	40	44.2	0.48368	0.55014	-0.32980
	FCW	22	40	44.2	0.48369	0.55018	-0.32990
HO PH	NCW	26	40	52.1	0.47122	0.53627	-0.32220
	FCW	26	40	52.1	0.47875	0.54536	-0.32560

EO PH (Elliptic Orbit Peak Heating)
HO PH (Hyperbolic Orbit Peak Heating)
NCW (Non-Catalytic Wall)
FCW (Fully Catalytic Wall)
* pole @ vehicle nose

As one can see, CFD computations (both Euler and Navier-Stokes) have been performed, both in trajectory-based and space-based design approaches [3]. Several Mach numbers and different angles of attack (α), have been investigated and compared.

The Fluent code together with user defined functions (UDFs), developed in order to simulate mixtures of gas in thermo-chemical non-equilibrium, have been used for CFD computations with a non equilibrium chemical model suitable for Martian atmosphere.

Note that, for the perfect gas case, the Mars atmosphere is characterized by a specific heat ratio γ (e.g., 1.3755) very close to that of Earth (e.g., γ=1.4). Therefore, it follows that force coefficients are nearly independent of CO_2 concentration and are essentially the same as those obtained using air [3].

For the reacting gas computations, the Martian atmosphere has been considered as a mixture of 95.7% carbon-dioxide, 1.6% Argon and 2.7% nitrogen. The flow has been modelled as a reacting gas mixture of 9 species (Ar, CO_2, N_2, O_2, CO, NO, N, O) involved in the chemical reactions of Table 2 [7], [8]. The reaction mechanism and the related chemical kinetics, taken into account in the present work, are summarized in Table 2, where M is the reacting partner (third body) that can be any of the nine reacting species of the gas mixture.

Table 2. *Reactions mechanism and rate parameters [8].*

Reaction	Third Body M	A_r $[cm^3mol^{-1}s^{-1}]$	β_r	T_d [K]
$CO_2+M \rightarrow CO+O+M$	***CO_2,CO,N_2,O_2,NO***	6.9×10^{21}	-1.5	63275
	Ar	6.9×10^{20}		
	C,N,O	1.4×10^{22}		
$CO+M \rightarrow C+O+M$	***CO_2,CO,N_2,O_2,NO***	2.3×10^{20}	-1.0	129000
	Ar	2.3×10^{19}		
	C,N,O	3.4×10^{20}		
$N_2+M \rightarrow N+N+M$	***CO_2,CO,N_2,O_2,NO***	7.0×10^{21}	-1.6	113200
	Ar	7.0×10^{21}		
	C,N,O	3.0×10^{22}		
$O_2+M \rightarrow O+O+M$	***CO_2,CO,N_2,O_2,NO***	2.0×10^{21}	-1.5	59750
	Ar	3.0×10^{21}		
	C,N,O	3.0×10^{22}		
$NO+M \rightarrow N+O+M$	***CO_2,C,N,O,NO***	1.1×10^{17}	0.0	75500
	Ar	5.0×10^{15}		
	CO,N_2,O_2	5.0×10^{15}		
C_2+M → C+C+M	***All***	2.0×10^{21}	-1.5	59750
NCO+M → CO+N+M	***All***	6.3×10^{16}	-0.5	24000
$NO+O \rightarrow N+O_2$		8.4×10^{12}	0.0	19450
$N_2+O \rightarrow NO+N$		6.4×10^{17}	-1.0	38370
$CO+O \rightarrow C+O_2$		3.9×10^{13}	-0.18	69200
$CO_2+O \rightarrow CO+O_2$		2.1×10^{13}	0.00	27800

Nonequilibrium computations have been performed since one of the most challenging problem facing the design of atmospheric entry vehicle is the phenomenon of "real gas behaviour". At hypersonic speeds, the shock wave produced ahead of the vehicle suddenly elevates the gas temperature in the shock layer. So the gas thermal energy may be comparable with the energy associated with a whole range of gas chemical processes such as: molecular vibrational excitation; dissociation of atmospheric molecules into their atomic forms; formation of other chemical species through recombination reactions; and ionisation of both molecular and atomic species [9]. Since the ratio between the specific heats (γ) depends on the number of active degrees of freedom (dof) of the species, it follows that, as the temperature increases, γ can not be considered as a constant (perfect gas hypothesis). Therefore, the gas mixture has to be considered in thermal and chemical non-equilibrium.
Finally, the CFD analysis of the MBS have been preceded by a code validation phase performed considering the available numerical and experimental data for the Mars Pathfinder probe at entry peak heating conditions [10], [11].

4.1 Mars Pathfinder

As an example of the results provided by the validation phase, contours of CO_2 mass fractions are reported in Figure 3.

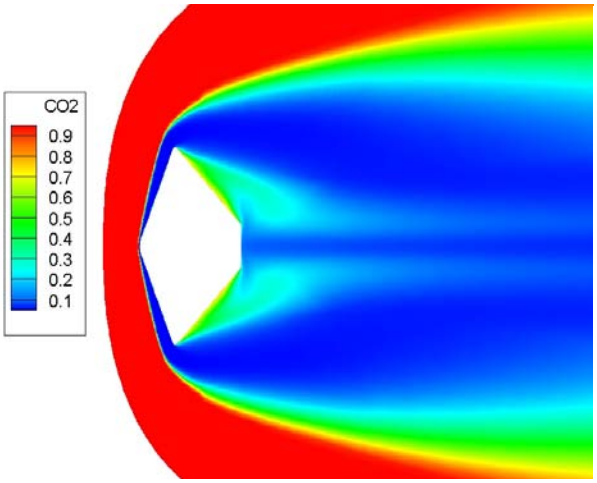

Figure 3. *Mars Pathfinder. Contours of CO_2 mass fraction.*

As shown, due to the strong bow shock ahead of capsule CO_2 completely dissociates except in the recirculation zones after the capsule shoulder where the flow separates [12], [13].
Figure 4 shows Mach number contours comparison between the perfect gas and the equilibrium flow results, while Figure 5 reports the same comparison for the static temperature contours. Flowfield streamlines are also shown in order to highlight the vortex structures which arise on the capsule leeside [13].

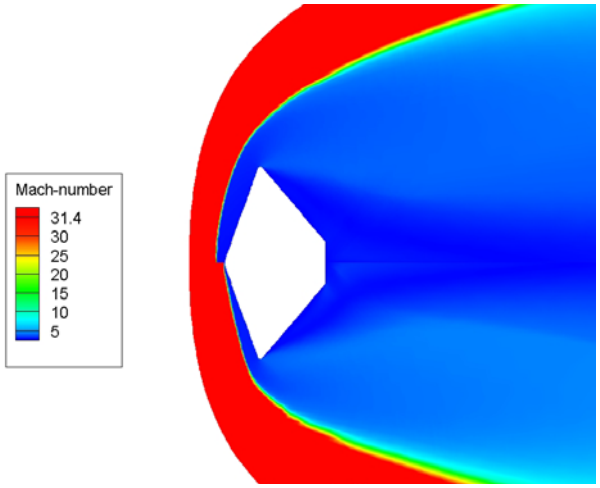

Figure 4. *Mars Pathfinder. Mach number contours. Comparison among perfect gas (upper side) and equilibrium flow.*

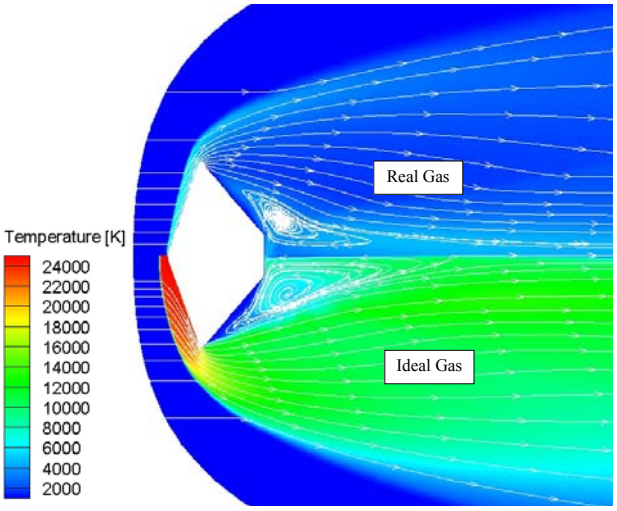

Figure 5. *Mars Pathfinder. Temperature contours. Comparison among equilibrium flow (upper side) and perfect gas computation.*

Finally, Figure 6 recognizes the comparison of surface pressure to stagnation pressure ratio

between present computation and results of [13], as evaluated on the capsule centreline.

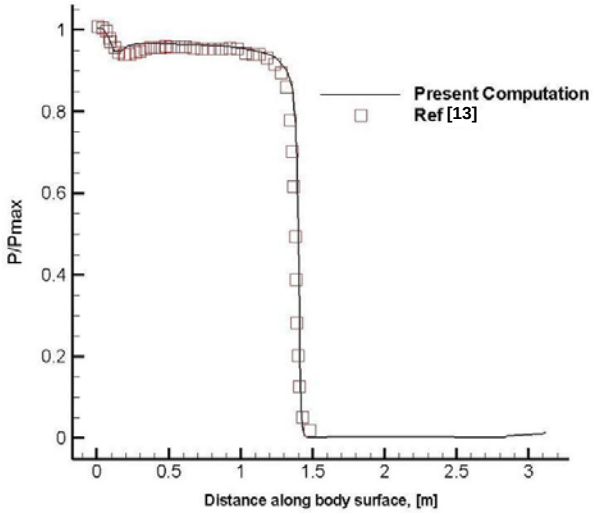

Figure 6. *Mars Pathfinder. Comparison of surface pressure to stagnation pressure ratio between present results and results of [13].*

As one can see, the comparison highlights a good agreement between numerical and experimental data

4.2 Numerical Results

The aerodynamic analysis of MBS is shown in term of lift (C_L), drag (C_D) and pitching moment (C_{My}) coefficients which are calculated according to Eq.(1) and Eq.(2), respectively.

$$C_i = \frac{F_i}{\frac{1}{2}\rho_\infty v_\infty^2 S_{ref}} \qquad i = L,D \tag{1}$$

$$C_{M\,j} = \frac{M_j}{\frac{1}{2}\rho_\infty v_\infty^2 L_{ref} S_{ref}} \qquad j = Y \tag{2}$$

The reference parameters L_{ref} (e.g., longitudinal reference length) and S_{ref} (e.g., reference surface) that have been chosen for the definition of the aerodynamic forces and moment non-dimensional coefficients are the capsule diameter (e.g., 5.0 m) and the vehicle length (e.g., 8 m), the maximum cross-section area of the VP ARES C (e.g., 19.6 m^2) and the VP ARES LB planform area (e.g., 32 m^2), respectively. The pitching moment is computed from the nose of the vehicle (i.e. 0,0,0).

4.2.1 Engineering-based results

Engineering based aerodynamic and aerothermodynamic analyses have been extensively performed by using a 3D Panel Methods code developed by CIRA (SIM, Surface Impact Method, namely also HPM) in the framework of its research activities on preliminary design of reentry vehicles. This tool, at high supersonic and hypersonic speeds, is able to accomplish the aerodynamic and aerothermodynamic analyses of a complex re-entry vehicle configuration by using simplified approaches as local surface inclination methods and approximate boundary-layer methods, respectively. The SIM typical of hypersonics are: Newtonian, Modified Newtonian, and Prandtl-Mayer theories [9]. In Figure 7 and Figure 8 typical surface meshes of the MBS, used for the engineering level computations is shown for the VP ARES C and LB vehicle, respectively.

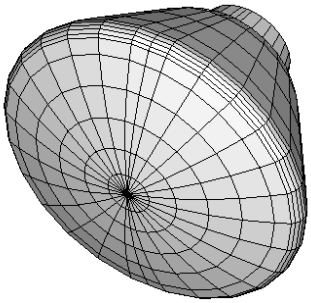

Figure 7. *The MBS panel mesh. VP ARES C.*

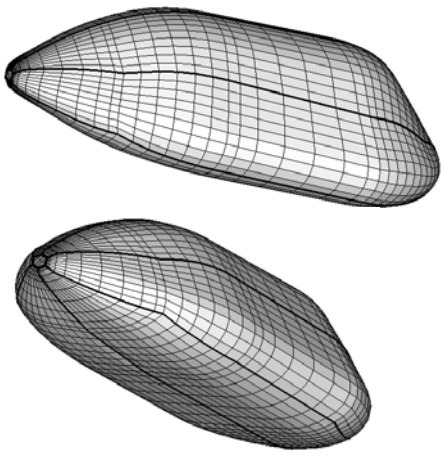

Figure 8. *The MBS panel mesh. VP ARES LB.*

MBS aerodynamic results provided by engineering-based analysis cover α ranging from 130 to 180 deg for the VP ARES C and 0 to 50 deg for the VP ARES LB.

As an example of SIM results, Figure 9 shows the curves of lift, drag, and aerodynamic efficiency thus representing the preliminary aerodynamics assessment of the Mars entry capsule.

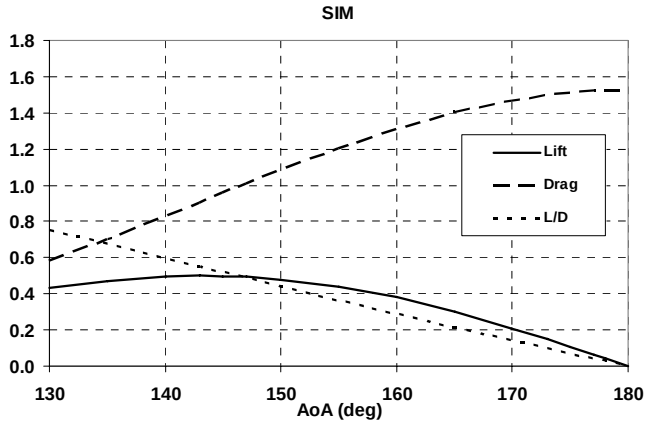

Figure 9. *Lift, drag, and L/D ratio coefficients versus α. Panel methods results.*

4.2.2 CFD-based results

Present CFD computations for the MBS have been carried out on a 3-D multiblock structured grid close to that shown in Figure 10. All the computational domains have been generated by means of the commercial tool ICEM-CFD.

The grid for the VP ARES C consists of 62 blocks for an overall number of 829.000 cells (half body) while that for LB configuration is made of about 20 blocks and 900.000 cells (half body). Both computational domains are tailored for the free-stream conditions of Table 1.

The distribution of surface grid points has been dictated by the level of resolution desired in various areas of the vehicle such as the stagnation region and the base fillet one, according to the computational scopes. Figure 10 shows a close-up view of the 3-D mesh on the vehicle surface (both capsule and lifting body) and on the VP ARES C pitch plane. Grid refinement in strong gradient regions of flowfield has been made through a solution adaptive approach. The preliminary results of CFD simulations performed so far are summarized hereinafter.

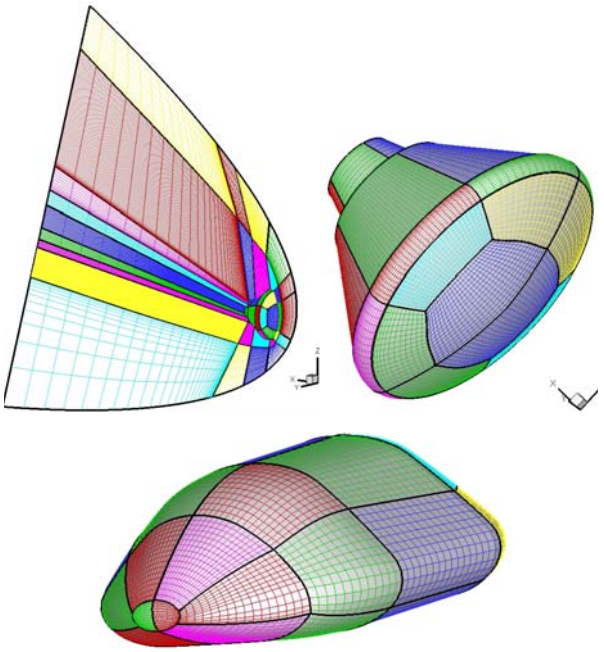

Figure 10. *The Computational mesh domains.*

For example, Figure 11 shows the static temperature contours on the capsule symmetry plane and two flowfield cross sections together with the Static pressure contours on capsule surface at M_∞=20 and α=20 deg, considering the Mars atmosphere as a perfect gas [3].

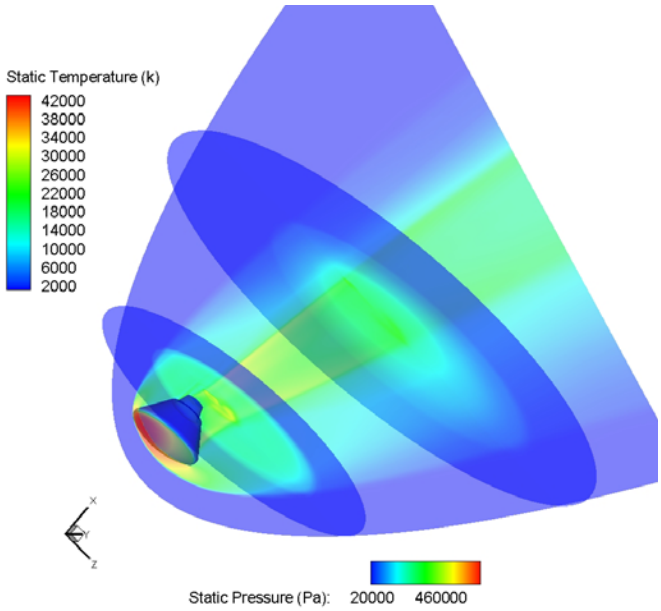

Figure 11. *The Static temperature field on the capsule symmetry plane and on two flowfield cross sections at M_∞=20 and α=20 deg. Static Pressure contour on capsule forebody* [3].

As shown, the MBS bow shock structure around the descent vehicle can be appreciated as well. At the same flight conditions, Figure 12 reports the static temperature contours for reacting gas computations. Departure from perfect gas behavior significantly affects the shock wave structure, and hence the flowfield around the vehicle [10], [3].

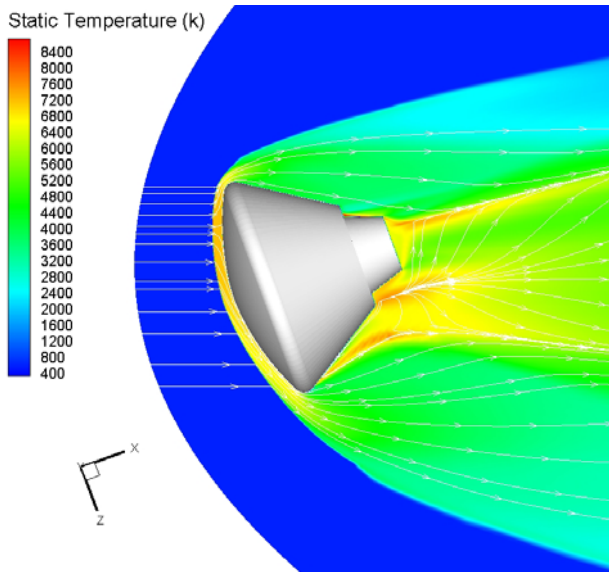

Figure 12. *Static temperature contours for M_∞=20 and α=20 deg. Non-equilibrium gas computation at M_∞=20 and α=20 deg* [3].

By comparing Figure 11 and Figure 12 one can realize that the static temperature in the shock layer due to species dissociation decreases up to about 7000 (K). The chemical dissociation of the flow in the shock layer can be recognized in Figure 13 where contours of both CO_2 and N_2 mass fractions on MBS pitch plane for M_∞=20 and α=20 deg are reported.

As a consequence, flow dissociation determines a large density ratio ε across the strong bow shock compared with a flow of the same gas where no dissociation takes place [9]. This results in a thinner shock layer around the entry vehicle (e.g., lower stand-off distance). Under conditions where dissociation exists, the aerodynamics of vehicle depends primarily on shock density ratio. In fact, the change of aerodynamic characteristics is the result of change in surface pressure acting on the vehicle forebody [11].

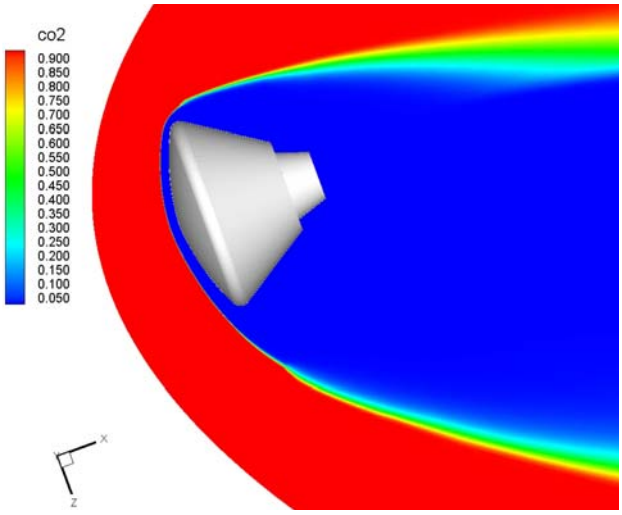

(a) CO_2

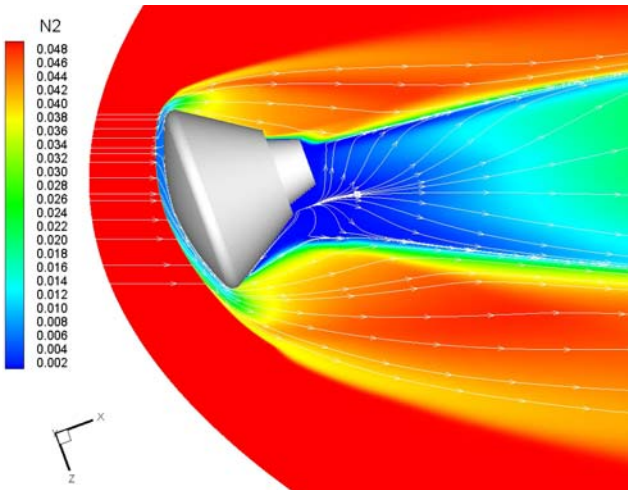

(b) N_2

Figure 13. *Contours of CO_2 and N_2 mass fractions on MBS pitch plane for M_∞=20 and α=20 deg* [3].

As matter of fact, the level of pressure at the vehicle stagnation point (e.g. Cp_{max}) reads:

$$C_{p\max} = C_{pt2} = \frac{P_{t2} - P_\infty}{q_\infty} = \left(\frac{P_{t2}}{P_\infty} - 1\right)\frac{2}{\gamma M_\infty^2} \cong 2 - \varepsilon \qquad (3)$$

instead of the classical newtonian value (e.g., Cp_{max}=2). Moreover, the density ratio across the bow shock wave, ε, in the hypersonic limit is:

$$\varepsilon = \lim_{M_\infty \to \infty} \frac{\rho_1}{\rho_2} = \frac{\gamma - 1}{\gamma + 1} \qquad (4)$$

So, ε changes as γ depends on the number of active dof of the gas mixture species.

The curves of lift, drag, and of pitching moment coefficients are shown in Figure 14. Both those figures collect MBS aerodynamic coefficients compared with some experimental data, reported in order to highlight accuracy of both numerical and engineering-based results [14].

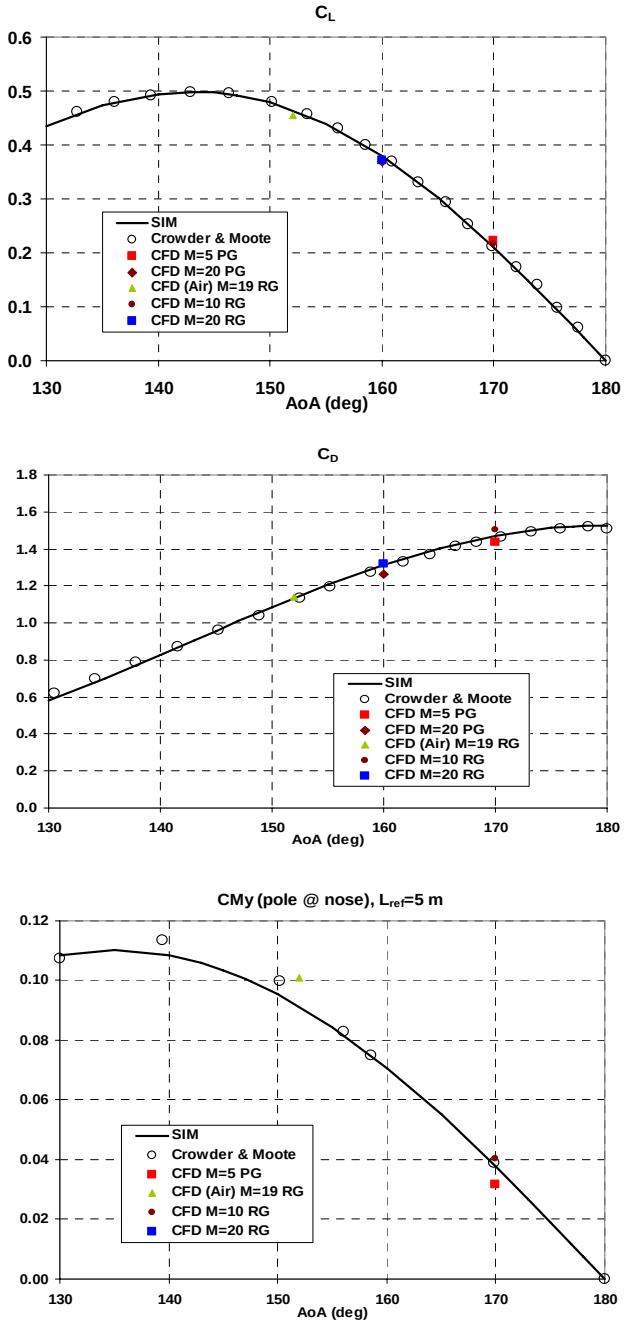

Figure 14. *Lift, Drag and pitching moment coefficients versus α. Comparison between panel methods, CFD results and experimental data [14].*

As one can see, experimental and numerical data compare very well, thus confirming that engineering-based estimations represent reliable preliminary aerodynamics of a Mars entry capsule. As a result, real gas effects increase both the aerodynamic drag and pitching moment coefficient, whereas the lift is only slightly influenced.

Note that, Figure 14 reports the Crowder-Moote and CFD results (CFD air M=19 RG) available for the Apollo capsule in air since, as said before, the static coefficients available for the air adequately represent the static coefficients for an aerodynamic braking vehicle in the Mars atmosphere [4].

As far as CFD results for VP ARES LB are concerned, Figure 15 and Figure 16 show the Mach number contours field that takes place around the vehicle when it is flying at the peak heating conditions of entry by EO (e.g., M_∞=22, α=40 deg, and H=44.20 km).

In particular, Figure 15 shows the Mach contours field on the vehicle pitch plane while Figure 16, together with Figure 15, gives an idea of the bow shock shape that envelopes the vehicle since the Mach field is reported on three different flowfield cross sections.

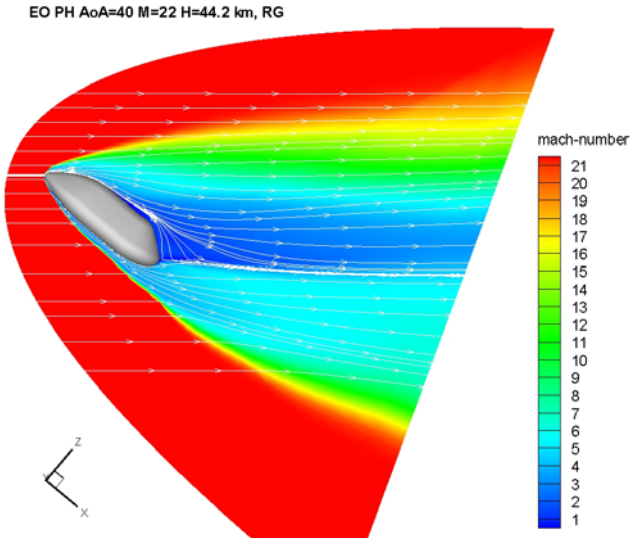

Figure 15. *Mach number contours field on the VP ARES LB pitch plane at the EOPH conditions (see Table 1).*

As shown, a thin shock layer envelopes the entry vehicle with a strong expansion that characterizes the windside flow at the end of vehicle.

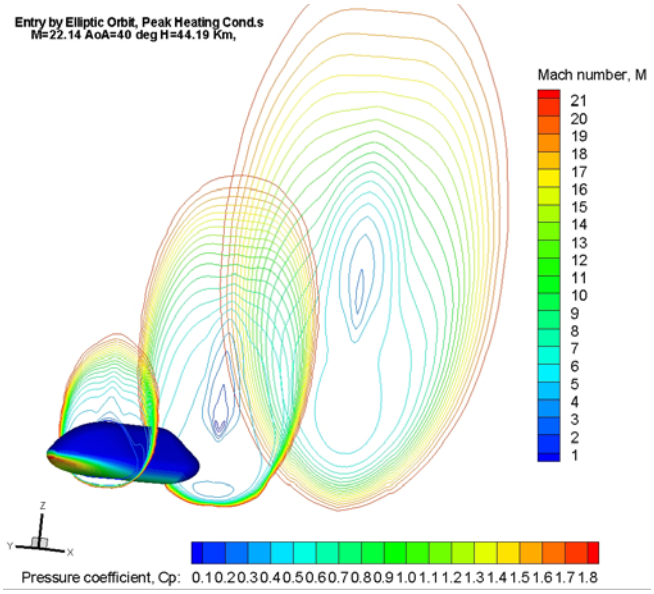

Figure 16. *Mach number field at the EOPH conditions on three flowfield cross section.*

The CO mass fraction field around the VP ARES LB for the same freestream conditions is shown in Figure 17 where some streamtraces colored by Mach number are also reported.

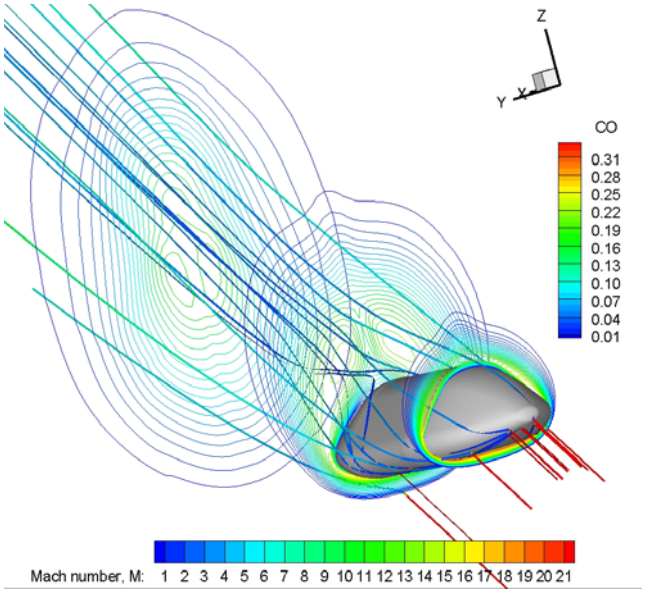

Figure 17. *CO mass fraction field at the EOPH conditions on three flowfield cross section with streamtraces colored by Mach number.*

As shown the CO concentration reaches its maximum value close to the body. Figure 18, Figure 19 and Figure 20 show the temperature comparison among nonequilibrium flow (right side of pilot) and perfect gas computation, evaluated at three flowfield cross sections (x=1.5 m, 5.5 m and 9.5 m).

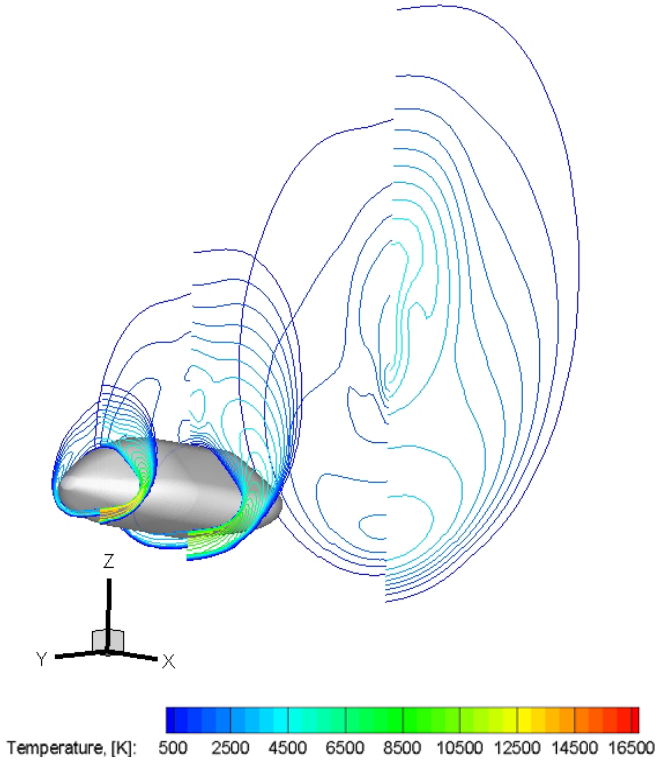

Figure 18. *Temperature comparison among non-equilibrium flow (right side of pilot) and perfect gas computation, at x=1.5 m, 5.5 m and 9.5 m flowfield cross sections.*

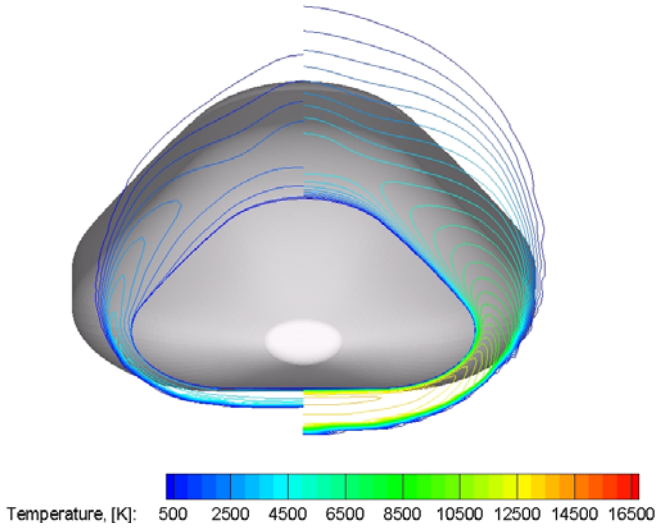

Figure 19. *Temperature comparison among non-equilibrium flow (right side of pilot) and perfect gas computation, at x=1.5 m flowfield cross section.*

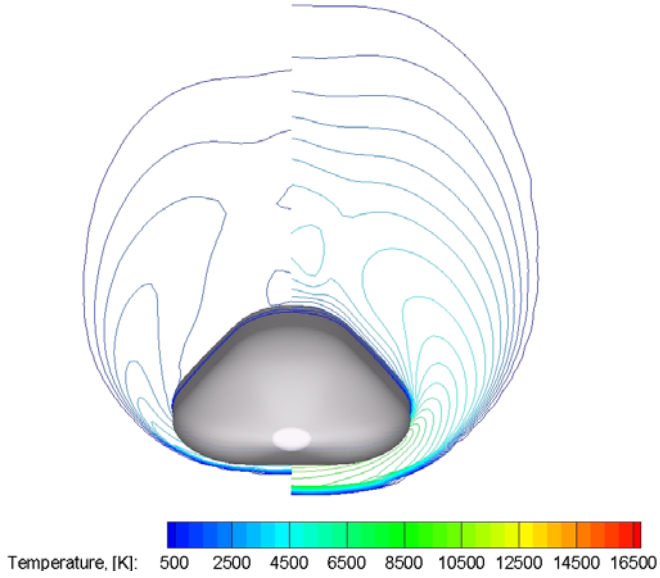

Figure 20. *Temperature comparison among non-equilibrium flow (right side of pilot) and perfect gas computation, at x=5.5 m flowfield cross section.*

It is clearly evident how real gas phenomena affect the vehicle shock layer, thus confirming all the conclusions highlighted before for the VP ARES C vehicle.
Figure 21 shows the temperature field on the vehicle pitch plane at HOPH freestream conditions (see Table 1).

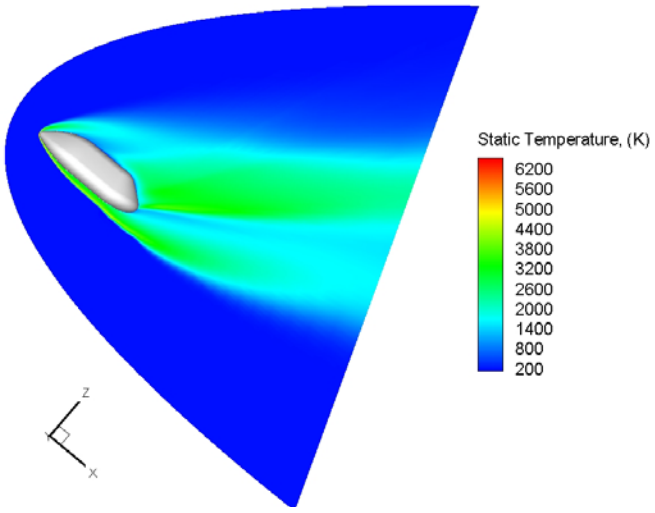

Figure 21. *Temperature contours field on the vehicle pitch plane at HOPH freestream conditions. M_∞=26, α=40 deg, and H=52.1 km.*

The flow passing through the bow shock wave reaches about 6000 (K) when the vehicle is flying at M_∞=26, α=40 deg, and H=52.06 km altitude). Finally, the curves of lift, drag, and pitching moment coefficients are shown in Figure 22. Real gas effects increase both drag and pitching moment coefficients, whereas the lift is only slightly influenced. VP ARES LB aerodynamics is also summarized in Table 1.

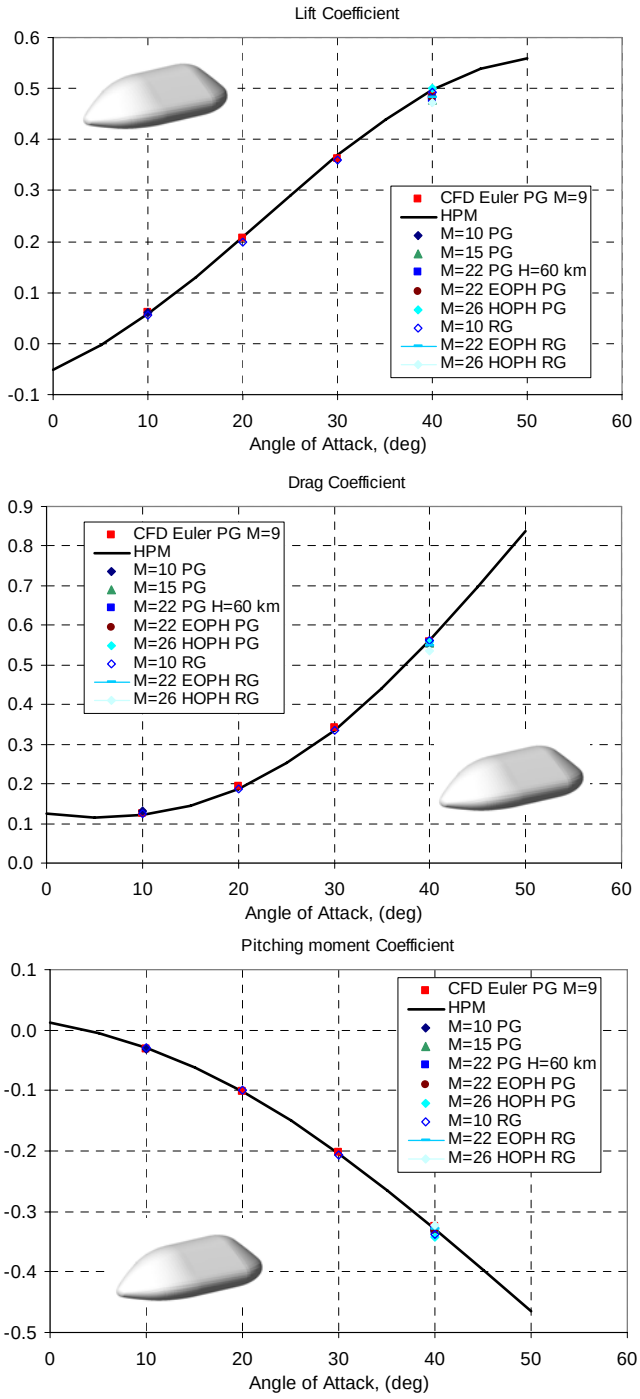

Figure 22. *VP ARES LB. Lift, Drag and pitching moment coefficients versus α. Comparison between panel methods and CFD results for perfect and non-equilibrium gas computations.*

As far as vehicle aeroheating is concerned, several Navier-Stokes computations have been performed assuming chemically reacting gas model, considering alternatively the heat shield surface as NC and FC wall (see Table 1). All the computations refer to fully laminar nonequilibrium flow conditions with vehicle surface temperature fixed at 300 K (cold wall condition hypothesis). No radiation heat flux and no heat shield ablation and recession were assumed for simplicity.

It is worth noting that, apart from the usual "no-slip" and zero normal pressure gradient boundary conditions at the wall, mass and energy balance equations are necessary to represent the interaction of the gas and surface (e.g., heterogeneous reactions) [9].

The mass balance equations are obtained considering that the flux due to mass diffusion is balanced by the production of molecular species through recombination of atoms:

$$\vec{J}_{s_w} \cdot \hat{n}_w = \rho_{s_w} \gamma_{s_w}(T_w) \sqrt{\frac{\Re T_w}{2\pi M_s}} \qquad (5)$$

where γ_s is the recombination coefficient.

When γ_s=1, it means that the wall permits complete recombination of atoms arriving at the surface (e.g., Fully Catalytic Wall – FCW). If γ_s=0, the surface does not permit recombination and it is said to be non-catalytic (NCW). As a consequence the heat released due to recombination at wall is a maximum for a FCW, and zero for a NCW [9], [15]. For a real thermal protection material (TPM), however, the recombination coefficients lie between these two extremes, i.e., $0 \le \gamma_s \le 1$ and are characteristic of that material.

Further, recombination coefficients are functions of temperature, i.e., $\gamma_s = \gamma_s(T)$. As preliminary TPS design criteria, the conservative assumption of a FCW is preferred since one can expect maximal heat release from recombination. Therefore, the energy balance equation at the cold wall surface, neglecting in-depth conduction through the TPS, reads:

$$\dot{q}_w = -k_w \vec{\nabla} T \cdot \hat{n}_w + \sum_{s=1}^{n_s} h_s(T_w) \vec{J}_{s_w} \cdot \hat{n}_w \qquad (6)$$

To illustrate the high temperature real gas effects on vehicle aeroheating, Figure 23 shows the comparison of heat flux on the centreline of the VP ARES LB vehicle, among the cases of PG and chemical nonequilibrium gas for both NCW and FCW boundary conditions.

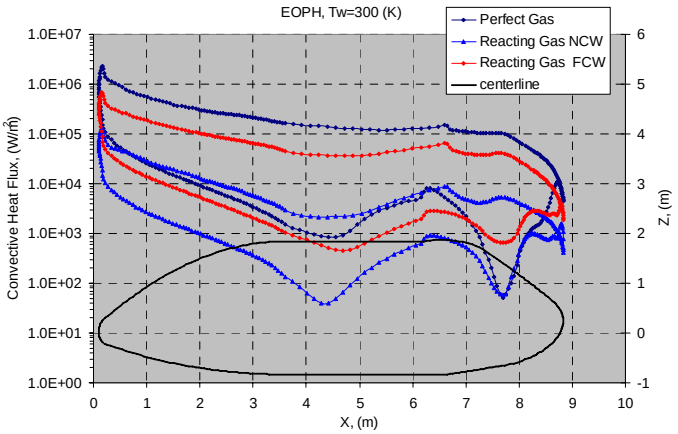

Figure 23. *VP ARES LB. Effect of chemical kinetics and wall catalyticity on vehicle heat flux. EOPH conditions (see Table 1).*

As one can see, the wall heat flux is higher in the case of PG condition. This can be explained considering that, as the vehicle surface is assumed as cold, the PG heat flux distribution is close to that of a chemical equilibrium computation. In this latter case, in fact, atoms recombine and liberate their energy of dissociation to the gas in the boundary layer (BL) still. On the contrary, when the BL is in chemical non-equilibrium, CFD simulations confirm that the higher heat flux is attained for FCW. As shown, this value is lower than that for PG, but is very large compared with the case of NCW. In particular, Figure 23 highlights that, at the EOPH conditions, the FCW to NCW heat flux ratio is equal to about 5.

5 Concluding Remarks

The paper deals with the aerodynamic and aerothermodynamic analysis of a manned braking system for manned exploration mission to Mars. A number of fully 3D Navier-Stokes and Euler CFD computations of the hypersonic flowfield past an Apollo-shaped capsule and a lifting body vehicle have been performed for

several freestream conditions of a proposed Mars entry loading environment. These evaluations have been aimed at carrying out only a preliminary design of the MBS configuration, in compliance with the Phase-A design level. The range between Mach 2 and Mach 26 has been analyzed, to provide both aerodynamic and aerothermodynamic databases according to both the "space-based" and "trajectory-based" design approaches.

Numerical results show that real gas effects increase both the aerodynamic drag and pitching moment coefficient, whereas the lift is only slightly influenced.

Moreover, wall catalyticity plays a fundamental role within a Mars entry since CFD results show that at the EOPH the ratio between FCW and NCW heat flux is equal to about 5.

References

[1] The site for the Mars Reference Mission: http://www_sn.jsc.nasa.gov/marsref/contents.html.

[2] G. Polishchuka, K. Pichkhadzea, V. Vorontsovb, K. Pavela, "Proposal on application of Russian technical facilities for International Mars Research Program for 2009–2015", Acta Astronautica, Vol. 59, pp.113-118. 2006.

[3] A. Viviani and G. Pezzella, "Aerodynamic Analysis of a Capsule Vehicle for a Manned Exploration Mission to Mars". 16th AIAA/DLR/DGLR International Space Planes and Hypersonic Systems and Technologies Conference. Bremen Oct. 2009. AIAA-2009-7386.

[4] G. M., Hanley, F. J. Lyon, "The Feasibility of Spacecraft Deceleration by Aerodynamic Braking at the Planet Mars", Proc. of the 1th AIAA Annual Meeting . Washington, D.C. June 29- July 2, 1964. AIAA-64-479.

[5] R. Gupta, K. Lee, C. Scott, "Aerothermal Study of Mars Pathfinder Aeroshell", Journal of Spacecraft and Rockets, vol.33 No 1, Jan.-Feb. 1996.

[6] A. Mack, "CFD Validation for CO_2 Reentry Applications", 2nd Inter. ARA Days. Arcachon, France, 21-23 October 2008. AA-3-2008-37.

[7] E.V. Kustova, E.A. Nagnibeda, Y. D. Shevelev, N.G. Syzranova, "Comparison of Non-Equilibrium Supersonic CO2 Flows with Real Gas Effects near a Blunt Body", Proc. Of the 6th European Symposium on Aerothermodynamics for Space Vehicles. Versailles, France. 3-6 Nov. 2008 – ESA SP-659, January 2009.

[8] C. Park, J. T. Howe, R. L. Jaffe, G. V. Candler, "Review of Chemical-kinetic Problems of Future NASA Missions, II: Mars Entries", Journal of Thermophysics and Heat Transfer, vol. 8, No 1, pp. 9-23, Jan-Mar 1994.

[9] Anderson, J. D., Hypersonic and High Temperature Gas Dynamics, McGraw-Hill Book Company, New York, 1989.

[10] P. Gnoffo, R. Braun, K. Weilmuenster, R. Mitcheltree, W. Engelung, R. Powell, "Prediction and Validation of Mars Pathfinder Hypersonic Aerodynamic Data Base", 7th AIAA/ASME Joint Thermophysics and Heat Transfer Conference. June 15-18, Albuquerque, NM (USA). 1998.

[11] P. Gnoffo, K. Weilmuenster, R. Braun, C. Cruz, "Influence of Sonic-Line Location on Mars Pathfinder Probe Aerothermodynamics", Journal of Spacecraft and Rockets, vol. 33 No 2, March-April 1996.

[12] V. Hannemann, A. Mack, "Chemical Non Equilibrium Model of the Martian Atmosphere", Proc. of the 6th European Symposium on Aerothermodynamics for Space Vehicles. Versailles, France. 3-6 Nov. 2008 – ESA SP-659, January 2009.

[13] R.A. Mitcheltree and P.A.Gnoffo, "Wake Flow about the Mars Pathfinder Entry Vehicle", Journal of Spacecraft and Rockets, vol.32 No 5, Sept.- Oct. 1995.

[14] Crowder, R. S., Moote, J. D., "Apollo Entry Aerodynamics", Journal of Spacecraft and Rockets, Vol. 6, No 3, 1969.

[15] A. Viviani, Pezzella, C. Golia, "Aerodynamic and thermal design of a space vehicle entering the Mars atmosphere" The Fifth International Conference on Thermal Engineering Theory and Applications. May 10-14, 2010 Marrakesh. Morocco.

Contact Author Email Address

antonio.viviani@unina2.it

Copyright Statement